A&A 399, 315–327 (2003)
DOI: 10.1051/0004-6361:20021789
© ESO 2003

Astronomy & Astrophysics

Doppler imaging of stellar surface structure

XIX. The solar-type components of the close binary σ^2 Coronae Borealis

K. G. Strassmeier[1,⋆] and J. B. Rice[2,⋆]

[1] Astrophysical Institute Potsdam, An der Sternwarte 16, 14482 Potsdam, Germany
e-mail: KStrassmeier@aip.de
[2] Department of Physics, Brandon University, Brandon, Manitoba R7A 6A9, Canada
e-mail: rice@BrandonU.ca

Received 18 October 2002 / Accepted 29 November 2002

Abstract. We present the first Doppler image for both stellar components of the F9+G0 ZAMS binary σ^2 CrB and found evidence for the coexistence of cool and warm spots on both stars. Cool spots appear mainly at polar or high latitudes while a confined equatorial warm belt appears on the trailing hemisphere of each of the two stars with respect to the orbital motion. We also present an update of the TempMap imaging code that allows us to solve the stellar surface temperature distribution on both binary components simultaneously, including photometric input. Several test reconstructions are performed to demonstrate its reliability and robustness. Our new orbital solution results in very precise masses for both components – good to 0.4% – and confirms the spectral classifications of F9 and G0 for the primary and secondary, respectively. The visual component, σ^1 CrB, seems to be G4 rather than G0. All three components are on or very close to the ZAMS which is also confirmed by the relatively high lithium abundance of about twenty times the solar abundance. Photometric light variations are detected with a period of 1.157 ± 0.002 days that we interpret to be the rotation period of both binary components. A $0\overset{\mathrm{m}}{.}04$ dimming in y together with a reddening of $0\overset{\mathrm{m}}{.}01$ in $b-y$ during the year 2000 suggests a long-term spot variability compatible with a period of at least 260 days.

Key words. stars: activity – stars: starspots – stars: imaging – stars: individual: σ^2 CrB – stars: late-type

1. Introduction

1.1. Surface imaging of solar-type stars and what does it tell us

One of the remaining obstacles in stellar astrophysics is the impact of a magnetic field onto an astrophysical plasma. The range of likely impacts spans from the super-strong fields of magnetars and their impact on the space-time structure near the neutron star's surface to the very weak but large-scale galactic field and its impact on star formation and evolution. In the present series of papers, we investigate the behavior of surface magnetic fields of stars with convective envelopes, i.e. dwarfs and giants in the mass range of 0.5–2.5 solar masses and with approximately solar effective temperatures. Solar analogy tells us that the surface spot distribution, and its variation in time, is a fingerprint of the underlying dynamo process and its subsequent magnetic-field eruption as bipolar sunspots or sunspot groups. On stars, we resolve the surface by an indirect tomographic imaging technique and map the surface temperature distribution as a proxy of the (predominantly radial) magnetic field. This requires high-resolution spectra well sampled over a rotation period of the star.

Up to now, various groups found large spots on or near the rotational pole (e.g. Hatzes & Kürster 1999; Strassmeier 1999; Collier-Cameron et al. 1999; Berdyugina et al. 1998; Barnes et al. 1998), differential rotation both in the same sense and in the opposite sense than on the Sun (Vogt et al. 1999; Donati & Collier-Cameron 1997; Hatzes 1998; Rice & Strassmeier 1996; Barnes et al. 2001), possibly detected meridional flows toward the pole (Weber & Strassmeier 2001; Strassmeier & Bartus 2000), detected and mapped prominences (Collier-Cameron et al. 1999) and warm spots (Piskunov 1996; Unruh et al. 1998; Strassmeier 1999), observed active longitudes and related activity flip-flops (Berdyugina et al. 1999), found spot evolution on very short- and on very long timescales (e.g. Washuettl et al. 2000; Barnes et al. 1998) and, finally, directly detected complex magnetic surface fields (Wade et al. 2000; Piskunov & Kochukhov 2001). The latter is still a rather virgin field because of a lack of appropriate spectro-polarimetric data.

In the present series of papers, we follow two approaches. Firstly, we try to enlarge the astrophysical parameter space with

Send offprint requests to: K. G. Strassmeier,
e-mail: KStrassmeier@aip.de

⋆ Visiting Astronomer, Canada-France-Hawaii Telescope, operated by the National Research Council of Canada, the Centre National de la Recherche Scientifique de France, and the University of Hawaii.

Article published by EDP Sciences and available at http://www.aanda.org or http://dx.doi.org/10.1051/0004-6361:20021789

new targets without a Doppler image. This should eventually lead to a relation between a surface spot distribution and a rotational or stellar-structure parameter, e.g. the rotation period or the Rossby number. Secondly, we try to monitor a few targets as continuously as possible, i.e. for decades, in order to detect a cyclic behavior of the surface spot distribution, and possibly *observe* a stellar butterfly diagram as the existence of such on a star is by no means certain (e.g. Messina & Guinan 2002). In the present paper, we present the first Doppler images for the close binary σ^2 Coronae Borealis.

1.2. The target

σ^2 CrB (TZ CrB, HD146361, $V = 5\overset{\mathrm{m}}{.}6$) is the brighter component of the visual binary ADS 9979 (the second component is σ^1 CrB 6.6″ away) with the orbital period of 1000 years. σ^2 CrB itself is a double-lined spectroscopic binary with a relatively short period of 1.14 days (Harper 1925; Tanner 1949; Bakos 1984; Duquennoy & Mayor 1991). For a summary of many more astrophysical data see the chromospherically active binary star catalog (Strassmeier et al. 1993) and more recently Osten et al. (2000, 2002). The light variability was discovered by Skillman & Hall (1978) and suggested a 0.1-day period. This period was confirmed by Percy (1980) but not by Bakos (1984). Later, Giménez et al. (1986) and Strassmeier et al. (1989) conclusively showed that it was spurious and that a period very similar to the orbital period was the correct one.

The primary star of σ^2 CrB is of spectral type F9-G0 and thus represents the "earliest" (spherical) star with a Doppler image so far. The secondary component is of G0-G1 type, and thus is not much different than the primary. Their convective envelopes are accordingly shallow and we could expect a significantly different flux-tube emergence than in a typical RS CVn-type binary. Donati et al. (1992) detected a clear signature of a magnetic field on the cooler component but not on the hotter. They found a Stokes V modulation that appeared restricted to the line-profile core rather than the line wings and thus speculated that the magnetic activity originated from high latitudes.

2. Observations

2.1. High-resolution spectroscopy

High-resolution spectroscopic observations were obtained with the *Gecko* Coudé spectrograph at the 3.6-m Canada-France-Hawaii telescope (CFHT) in two observing runs each two nights long in May 17–18, 2000 and May 21–22, 2000. This splitting of nights was mandatory in order to obtain full phase coverage because the orbital period (and the rotational periods) is 1.14 days, and thus close to the day-night cycle.

The Gecko spectrograph was used with the 316 l/mm grating in 9th order and provided a resolution of ≈120 000. The 4.4k×2k EEV1E CCD with 13.5 μm pixels provided a dispersion of 0.0017 nm/px and allowed for a useful wavelength coverage of around 8.0 nm centered at 642.5 nm. Seeing was always between 0.6–1.2″ and all integrations were set to an exposure time of 4×300 s and have typical signal-to-noise ratios of 150:1 per single exposure per pixel. We took a single Th-Ar comparison spectrum preceding every 4×300-s block on σ^2 CrB, and a series of five flat-field spectra from a quartz lamp preceding every fifth such block. The many comparison-star spectra enabled a very precise interpolation of the wavelength scale throughout the night, thus taking care of eventual CCD drift, non-linearities, and similar instrumental instabilities causing "external" errors. No such drift was noticeable during the reduction though. A few integrations were centered at 671.0 nm and separate Th-Ar spectra were obtained for this wavelength region. Calibration targets and some targets of interest were observed at this wavelength, among them the visual companion σ^1 CrB.

The above sequence allowed for a total of 256 spectra of σ^2 CrB, i.e. 64 combined spectra with S/N mostly above 300:1, each the sum of four individual integrations and well distributed over all rotational phases (see the log in Table 1). Eight of these spectra were eliminated from the analysis because they suffered from excessively low S/N due to clouds but are included in the radial-velocity measurements. Figure 1a displays a typical single-exposure spectrum during a double-lined phase. No water-vapor lines above the nominal noise level are obvious in the wavelength regions of interest and no attempts

Table 1. Example from the spectroscopic observing log and radial velocities.

HJD 2451000	Phase (Eq. (1))	v_r (km s^{-1})	Std.dev. (km s^{-1})	Observatory
Star 1				
682.768	0.415	–65.1	0.0	CFHT
682.772	0.419	–65.9	–0.1	CFHT
Star 2				
682.768	0.415	+40.7	0.0	CFHT
682.772	0.419	+42.0	–0.1	CFHT

Note: The full table is available in electronic form at the CDS via anonymous ftp to `cdsarc.u-strasbg.fr` (`130.79.128.5`) or via `http://cdsweb.u-strasbg.fr/cgi-bin/qcat?J/A+A/399/315`

Table 2. Astrophysical data for σ^2 CrB.

Parameter	Primary	Secondary
Distance (Hipparcos)	21.7 ± 0.5 pc	
Spectral type	F9V	G0V
M_V	$+4\overset{\mathrm{m}}{.}607 \pm 0\overset{\mathrm{m}}{.}065$	$+4\overset{\mathrm{m}}{.}764 \pm 0\overset{\mathrm{m}}{.}067$
Luminosity	1.167 ± 0.074 $L_\odot$	1.024 ± 0.068 $L_\odot$
log g	4.5 ± 0.2	4.5 ± 0.2
$< B-V >$	$0\overset{\mathrm{m}}{.}599 \pm 0.007$	
$T_{\rm eff}$	6000 ± 50 K	5900 ± 50 K
$v \sin i$	26 ± 1 km s^{-1}	26 ± 1 km s^{-1}
Rotation period	1.157 days	1.157 days
Radius	1.14 ± 0.04 $R_\odot$	1.10 ± 0.04 $R_\odot$
Inclination	28°	28°
Mass	1.108 ± 0.004 $M_\odot$	1.080 ± 0.004 $M_\odot$
Macroturbulence, ζ	4.5 km s^{-1}	4.5 km s^{-1}
Microturbulence, ξ	2 km s^{-1}	2 km s^{-1}

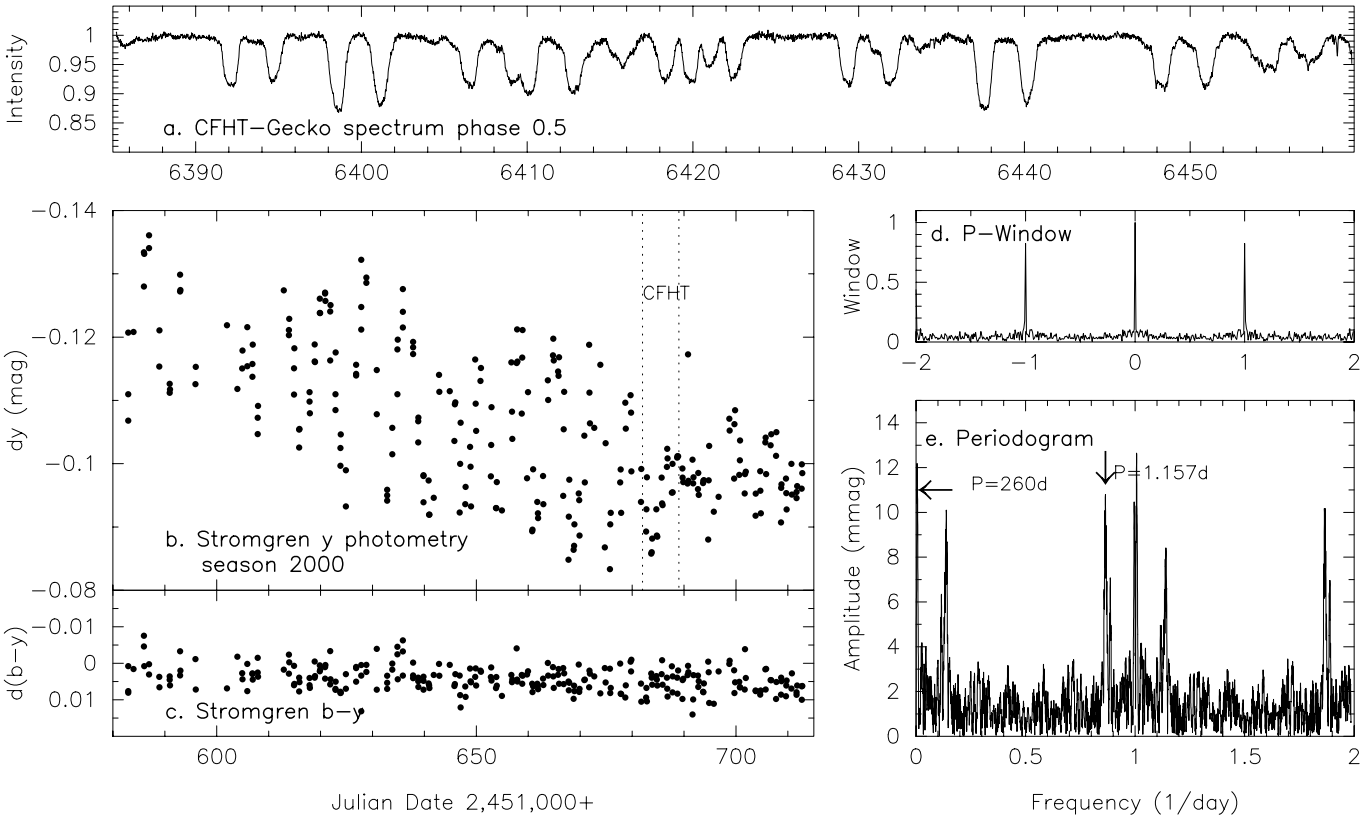

Fig. 1. a) Example spectrum of σ^2 CrB at phase 0.5. The spectral resolution of 120,000 and the phase resolution of 0.012 (integration time of 20 min) allows for an equivalent surface resolution of the Doppler images of $\approx 10°$ **b), c)** Season 2000 y and $b-y$ light and color variations of the combined $\sigma^2 + \sigma^1$ CrB light. All data were taken with the Wolfgang APT of the University of Vienna and obtained through a 30″ diameter aperture. **d), e)** Periodogram and window function from the data in panel b. A simultaneous two-frequency least-squares solution was used to find the best-fit periods.

were made to correct for it. The reduction procedure was nearly identical to that in our paper on HII 314 (Rice & Strassmeier 2001) obtained with the same instrumental set up and we refer the reader to that and previous papers in this series. A radial-velocity standard was observed at the beginning (β CVn) and at the end of each night (γ Ser) and provided the absolute zero point of our radial-velocity calibration.

2.2. Time-series photometry

Simultaneous and contemporaneous photometric observations were provided by Wolfgang, the blue-optimized 0.75-m telescope of the twin Vienna-Observatory Automatic Photoelectric Telescope (APT) at Fairborn Observatory in southern Arizona (Strassmeier et al. 1997). These observations cover the entire year 2000 observing season (Fig. 1b) with a sampling of three points per night and are still being continued. A total of 292 *by* measurements, each the mean of three 10-s readings per filter with an internal standard deviation of less than 7 mmag, constituted the useable data set for this paper. Measurements with a larger internal standard deviation were discarded. The average internal standard deviation throughout the observing season was 2.1 mmag.

All data were taken in and transformed to the Strömgren *uvby* system and used HD 143761 (G2V, $V = 5\overset{\mathrm{m}}{.}39$, ESA 1997) and HD 143435 (K5III) as the comparison and check star, respectively. A diaphragm of 30″ included both visual components of the σ CrB system, i.e. σ^1 CrB (G0V) and σ^2 CrB (F9V+G1V), but σ^2 is brighter than σ^1 by 1.1 mag in V. Nevertheless, the photometry must be corrected for the presence of the third light and this was done according to the formulae given in, e.g., Strassmeier & Bartus (2000). We remark though that this procedure relies on the assumption that σ^1 does not vary in light (as suggested from the spectrophotometric data of Frasca et al. 1997) .

2.3. Spatial resolution

With the current resolving power of $\lambda/\Delta\lambda = 120\,000$ ($\Delta\lambda$ of 0.0054 nm at 642.5 nm, or 2.5 km s^{-1}) and a full width of the lines at continuum level of $2\,(\lambda/c)\,v \sin i \approx 0.1070$ nm, we have a comfortable 20 resolution elements across the stellar disk. It translates into a theoretical spatial resolution along the equator at the stellar meridian of approximately 9°. The total time-on-target of 23 min (including CCD overhead) will cause phase smearing due to stellar rotation of up to a maximum of $0\overset{\mathrm{p}}{.}012$ or 4° along the stellar equator and in the direction of the rotational motion, thus well below the spectroscopic resolution limit. Additionally, the binary motion itself will cause a wavelength smearing of between practically zero at conjunction and

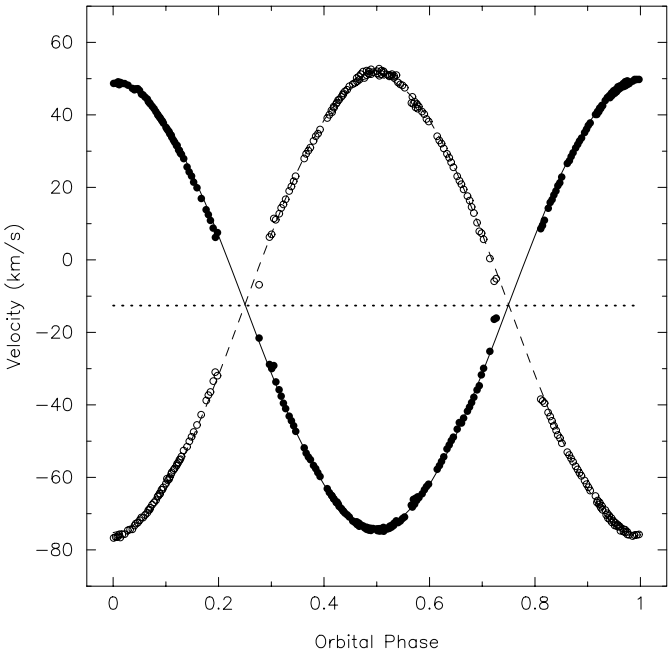

Fig. 2. Radial velocities and new orbit for σ^2 CrB. Filled circles denote the primary, open circles the secondary. The dotted line indicates the systemic velocity of –12.3 km s^{-1}.

a maximum of ±0.0075 nm at quadrature during the 23 minutes of integration. The lines from both components are sufficiently narrow to neglect differential wavelength smearing between the blue wing and the red wing of the line profile. At quadrature this effect amounts to 0.0002 nm or 0.01 km s^{-1}, thus does not affect our surface imaging.

Table 3. Improved orbital elements.

Element (Unit)	Value
$P_{\rm orb}$ (days)	1.1397912 (adopted)
T_0 (HJD)	2,451,683.4400
γ (km s^{-1})	-12.3 ± 0.06
K_1 (km s^{-1})	61.34 ± 0.06
K_2 (km s^{-1})	62.91 ± 0.08
e	0.0 (adopted)
$a_1 \sin i$ (km)	$0.96138 \pm 0.00093 \times 10^6$
$a_2 \sin i$ (km)	$0.9861 \pm 0.0012 \times 10^6$
a (i = 28°) (km)	4.148×10^6
$m_1 \sin^3 i$ ($M_\odot$)	0.1147
$m_2 \sin^3 i$ ($M_\odot$)	0.1118
mass ratio	0.975 ± 0.002
m_1 (i = 28°)($M_\odot$)	1.108 ± 0.004
m_2 (i = 28°)($M_\odot$)	1.080 ± 0.004
RMS for solution (km s^{-1})	0.71

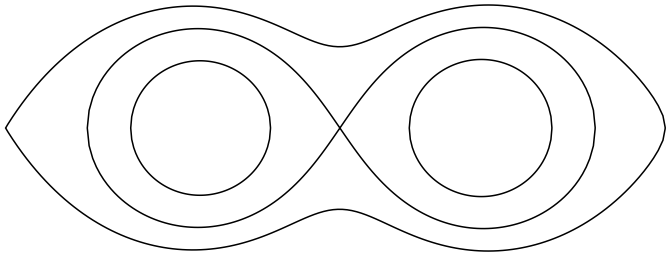

Fig. 3. Critical Roche equipotentials in the σ^2 CrB binary system. Shown are the stellar surfaces (inner circles) and the inner and outer critical equipotentials. Both components are close to spherical in shape.

3. Astrophysical parameters of σ^2 CrB

3.1. New high-precision spectroscopic orbit

A byproduct of the Doppler imaging is the accurate measurement of radial velocities for both stellar components. We obtained altogether 450 new velocities from the uncombined spectra (224 for the primary and 226 for the secondary) and used them to recompute the orbital elements. We did not add the previously published (photographic) velocities from Bakos (1984), taken between 1971–1983 (18 data points) and the original photographic data from Tanner (1949), nor the data from Duquennoy & Mayor (1991) (10 data points) because, firstly, they are much less precise than ours and, secondly, the orbital period is already well determined.

Our new velocities were obtained from cross correlations of the full 80-Å long spectrum with spectra of the IAU velocity standard β CVn (G0V, $v_{\rm r}$ = 6.33 km s^{-1}) and γ Ser (F6V, $v_{\rm r}$ = 6.58 km s^{-1}) and have external errors of as low as 0.1 km s^{-1} and as large as 1.2 km s^{-1}. The velocities are listed in Table 1 along with its O–C residuals from the orbital solution .

We gave all our unblended phases unit weight while the velocities from the fully blended phases (eleven measurements) were given zero weight. Final orbital elements were then derived with the updated differential-correction routine of Barker et al. (1967) as described and applied by Fekel et al. (1999). A first run with the elements from Bakos (1984) already converged at an eccentricity so close to zero that a formal zero-eccentricity solution was adopted. The improved elements are listed in Table 3 and the computed velocity curves are plotted in Fig. 2 along with the observations. Note the very precise masses, good to 0.4%.

All phases in this paper are computed with the new elements in Table 3.

3.2. Rotation period(s)

Starspots on the surface of a rotating star are ideal markers to determine the stellar rotation period to very high precision. In the case of σ^2 CrB, however, we have two (almost) identical stars that contribute to the observed light and to its variations. Any periodogram analysis of the total light will thus lead to an average period from the two stars (but see Kövari & Oláh 1996 for a possible numerical treatment). However, the observed period from the total light will be the rotation period for both components if the rotation is synchronized to the orbital motion. As we will show later, this is most likely the case for σ^2 CrB. Otherwise, our photometric data set would be long enough to see evidence for the existence of two close-together photometric periods, which we do not.

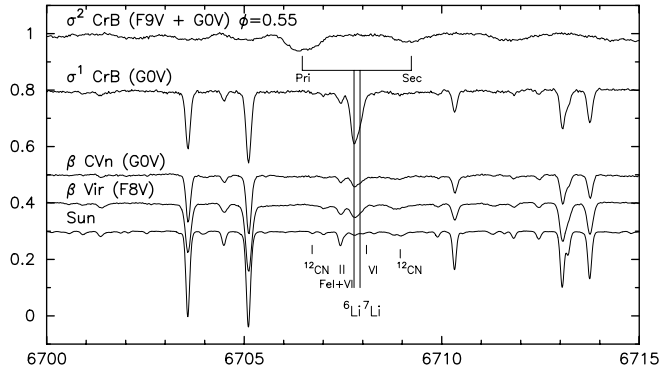

Fig. 4. Li I 670.8 nm spectra of both visual components of σ CrB (upper two spectra; all spectra except of σ^2 CrB are shifted in intensity for better presentation). The lower three spectra are comparison-star spectra of β CVn, β Vir, and the Sun. The two vertical lines indicate the wavelength of the two lithium isotope lines, dashes mark the various blends in the vicinity. A strong lithium line is detected in both components of σ^2 CrB and in σ^1 CrB.

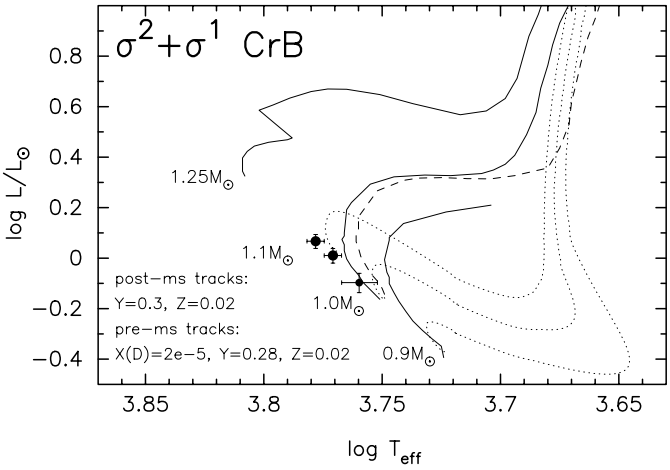

Fig. 5. The position of the σ^2 CrB primary and secondary components in the H-R diagram (primary: left dot; secondary: right dot; σ^1 CrB is marked as a smaller dot). The dotted lines are the pre-main-sequence tracks of D'Antona & Mazzitelli (1997) for masses of 0.9, 1.0, and 1.1 solar masses. The full lines are post-main-sequence tracks for 0.9, 1.0, and 1.25 solar masses from Schaller et al. (1992). The dashed line is the 1.0-$M_\odot$ track from Charbonnel et al. (1999) with a MHD equation of state. All tracks suggest masses of around 1.1 $M_\odot$ for σ^2 CrB.

We first carried out a Fourier analysis of the combined data in the b and y bands. The orbital period is by far the most significant in the data set. However, there is also a long-term trend in the data that must be considered real because the check- minus comparison-star magnitudes do not show this trend. Instead of prewhitening the data, we performed a multi-period search on the combined data and a subsequent two-period least-squares fit to minimize the residuals. Only two periods are required to achieve the best fit at a residual of $0\overset{\mathrm{m}}{.}007$ (Fig. 1e). The most significant period is 1.157 ± 0.002 days with an amplitude of $0\overset{\mathrm{m}}{.}035$ in y, i.e. within 1.5% of the orbital period. Several of its aliases, $1 - f$, $1 + f$, $2 - f$ etc., show up as significant periods as well, but the only second real period stems from the trend seen in Fig. 1b and appears to be compatible with a period of at least 260 days. Bakos (1984) already presented evidence of a 3.5 yr periodicity of the mean V magnitude, and Strassmeier et al. (1989) found a 2.0 yr period from early APT data. Whether this period is from one of the two σ^2 CrB components or from the G star in σ^1 CrB remains to be determined, e.g. with the spectrophotometric technique used by Frasca et al. (1997).

3.3. Asynchronism or differential rotation?

The difference of 0.0172 days (1.51%) between the photometric period and the orbital period is statistically significant (8.6σ). It could be interpreted as a slight asynchronism between the stellar rotation and the orbital revolution. A small orbital eccentricity in case of strict pseudosnychronism (e.g. Hall 1986) can be excluded because the photometric (= rotation) period is longer than the orbital period. Moreover, our orbital solution does not indicate an eccentricity larger than 0.01. Therefore, we believe that the difference of 1.5% is due to differential surface rotation rather than asynchronism. Differential rotation of this order is commonly observed on active cool stars (e.g. Hall 1991).

3.4. Sphericity of the components

We first estimate the average stellar radii from the relation $R \sin i = P(v \sin i)/50.6$. $V \sin i$ is determined from our high-resolution spectra by reconstructing the time-series line profiles in the 643.0 nm wavelength region from a set of trial inversions with $v \sin i$ as a "free" parameter. This yields $v \sin i$(F9) = 26.0 ± 1 km s^{-1} and $v \sin i$(G0) = 26.0 ± 1 km s^{-1} and, with $P_{\rm rot} = P_{\rm orb}$, gives $R \sin i$(F9) = 0.586 ± 0.022 $R_\odot$ and $R \sin i$(G0) = 0.586 ± 0.022 $R_\odot$. However, the line depth ratios in the 6430-Å region is best reproduced in the inversion with a ratio of the two stellar radii of 0.955, still within the error range of the minimum radii from $v \sin i$. In spite of the fact that the measuring error of $v \sin i$ dominates the uncertainty on the radius, it nevertheless allows us to compute a minimum stellar radius solely from observed quantities.

The Roche-lobe radius is determined from the semi-major orbital axis and the mass ratio m_j/m_{j+1} (j = 1, 2) and is for the primary ≈1.66 $R_\odot$ and for the secondary 1.64 $R_\odot$ (the stellar radii are approximately 1.14 and 1.10 $R_\odot$, respectively). Relative (mean) radii R/a are 0.192 and 0.185 for the primary and secondary, respectively, i.e. both stars fill a large fraction of their Roche lobe (≈30%) but are still significantly detached from their inner critical equipotential surfaces. The above relative radii and the mass ratio of 0.975 determine the equipotential surfaces and thus the various radii on the stellar surface(s). Figure 3 shows the location of the inner and outer critical equipotentials as obtained with the program BinaryMaker (Bradstreet 1993). From this, we find deviations from sphericity for both components of between 1.5% in the direction perpendicular to the major axis and 4.6% along the major axis toward L_1. As for the case of the double-lined close binary V824 Ara (Strassmeier & Rice 2000), we are confident that this is not enough to produce an effect on our line-profile modelling.

a. Artificial input image

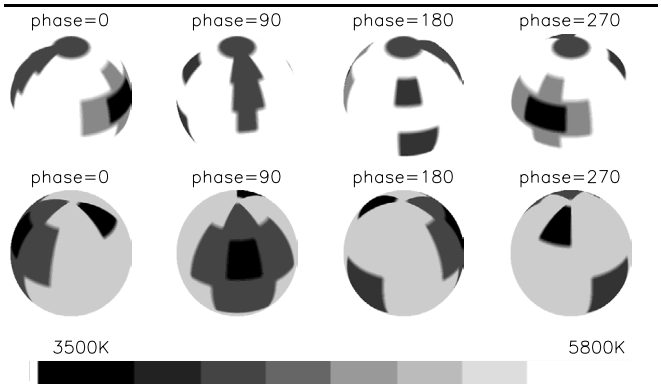

b. Recovered images without photometry

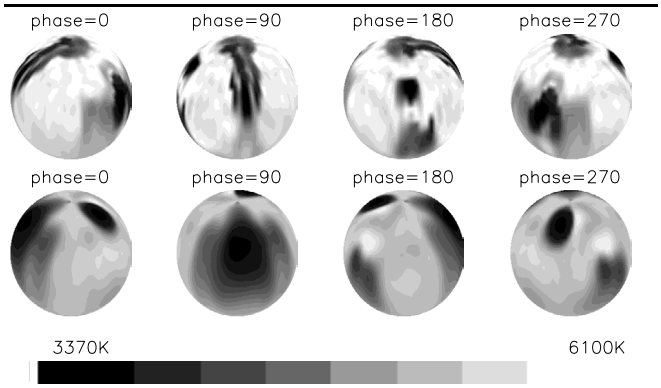

Fig. 6. Test of the two-star version of TempMap without photometric input. Top: Artificial input map for both components. Bottom: Reconstruction from 18 line profiles equally-spaced in phase but without photometric data.

a. Test with photometry and Tikhonov regularization

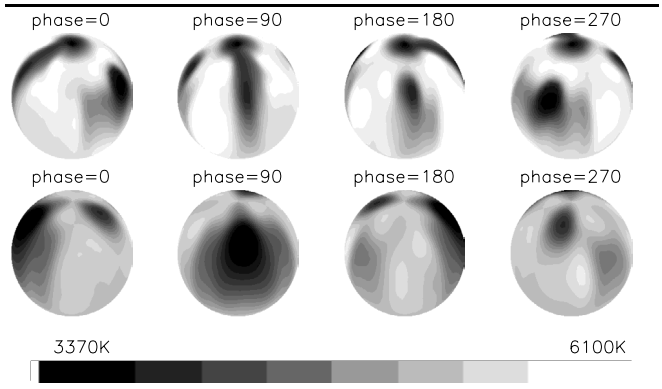

b. Test with photometry and MaxEnt regularization

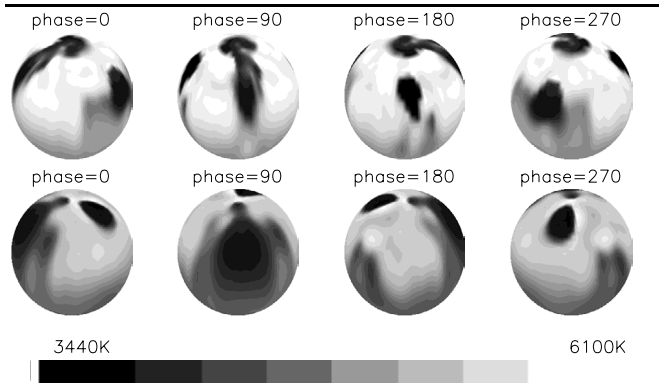

Fig. 7. Test of the two-star version of TempMap including two photometric bandpasses. Top: Tikhonov regularization. Bottom: Maximum entropy regularization.

3.5. Lithium abundances for both visual components

Figure 4 shows a representative high-resolution spectrum of the lithium 670.8-nm region for both visual components. The average equivalent width measured from these spectra, three in number for σ^2 CrB and two for σ^1 CrB, is 46.5 ± 3 mÅ and 42 ± 3 mÅ for the σ^2 primary and secondary, respectively, and 60 ± 2 mÅ for σ^1. The uncertainties quoted are rms errors from a fit with a double Gaussian to each stellar component, and based on a minimization of the residuals with a standard least-squares approach. This fit separates the Li I line from the nearby Fe blend. However, our abundance is still the sum from the two isotopes ^{6}Li and ^{7}Li. When using the non-LTE curves of growth of Pavlenko & Magazzú (1996) for a 6000 K/log g = 4.5 model for the primary and a 5900 K/log g = 4.5 model for the secondary, we derive Li abundances of 2.53 ± 0.05 and 2.40 ± 0.05 (on the log n(H) = 12.00 scale) for the primary and secondary of σ^2 CrB, respectively. For σ^1 CrB, we derive 2.60 ± 0.03 with the 5900-K model. The uncertainties quoted are the propagated errors from the measurement of the line equivalent width and do not include uncertainties from the effective temperature calibration. It is thus likely that the absolute abundances will be more uncertain.

3.6. Inclination of the rotational axes

Because photometry of σ^2 CrB has shown it to be a non-eclipsing system (Bakos 1984; Strassmeier et al. 1989), and because the orbital elements are now known to very high precision, the inclination of the orbital plane with respect to the line of sight must be lower than 45.6° ($R_1 + R_2$ must be less than $a \cos i$). On the other hand, an inclination of below ≈10° is unlikely because we detect significant rotational modulation in total light with a full amplitude of $0\overset{\mathrm{m}}{.}035$ in y and a moderately large $v \sin i$. In spite of the fact that numerical simulations (e.g. Strassmeier 1996) have shown that an amplitude of $0\overset{\mathrm{m}}{.}035$ can be obtained even at an inclination of as low as 5°, it would require a single spot as large as a hemisphere but without any flux contribution, something which is not supported by the observed line profiles. We therefore adopt an inclination of 30° for our initial Doppler imaging following Bakos (1984) who suggested an inclination of i = 28°.

Having determined the rotational velocity, the rotational period, and the luminosity class, we can further constrain and

check the inclination of the stellar rotation axis from the relation $R \sin i = P(v \sin i)/50.6$. The Landolt-Börnstein tables (Schmidt-Kaler 1982) list a radius for a G0V star of 1.10 $R_\odot$ and for a F9 star of 1.14 $R_\odot$ that translate into an inclination of $31-32^\circ \pm 2^\circ$ (again, only the error for $v \sin i$ was included).

3.7. Absolute dimensions and age

The parallax measurement by the *Hipparcos* satellite (ESA 1997) confined the distance of σ^2 CrB to 21.7 ± 0.5 pc. If we adopt the maximum (combined) visual brightness of $5\overset{\mathrm{m}}{.}605$ observed so far (this paper), the systemic absolute visual brightness is $M_V = +3.93 \pm 0.05$ mag. Equivalent widths were measured for three relatively unblended line pairs in our 643-nm spectra and yield an average line ratio of 1.156 ± 0.034 (rms), and accordingly a magnitude difference between the components of $\Delta m = 0\overset{\mathrm{m}}{.}16 \pm 0\overset{\mathrm{m}}{.}03$. The individual component's absolute magnitudes are thus $M_V(\mathrm{pri}) = +4\overset{\mathrm{m}}{.}607 \pm 0\overset{\mathrm{m}}{.}065$ and $M_V(\mathrm{sec}) = +4\overset{\mathrm{m}}{.}764 \pm 0\overset{\mathrm{m}}{.}067$, where ≈75% of the errors come from the parallax error. Adopting the bolometric corrections from Flower (1996), the luminosities are 1.167 ± 0.074 $L_\odot$ and 1.024 ± 0.068 $L_\odot$, respectively (with $M_{\mathrm{bol},\odot} = +4\overset{\mathrm{m}}{.}73$).

The corresponding values for σ^1 CrB are based on a magnitude difference ($\sigma^2 - \sigma^1$) of $-1\overset{\mathrm{m}}{.}12$ (with an uncertainty of $\pm 0\overset{\mathrm{m}}{.}05$). This value was obtained from the light curves of Frasca et al. (1997) and is the average maximum ΔR from their spectrophotometry in 1988 and 1989. The absolute visual magnitude is thus $+5\overset{\mathrm{m}}{.}05 \pm 0\overset{\mathrm{m}}{.}10$ and the luminosity just 0.80 ± 0.07 $L_\odot$, i.e. ≈G4.

Figure 5 shows the position of all three stellar components in the H-R diagram with respect to evolutionary tracks. The dotted lines are the pre-main-sequence tracks of D'Antona & Mazzitelli (1997) for 0.9, 1.0, and 1.1 $M_\odot$, the full lines are the post-main-sequence tracks of Schaller et al. (1992) for 0.9, 1.0, and 1.25 $M_\odot$, and the dotted line is the Charbonnel et al. (1999) track for 1.0 $M_\odot$. The latter differ mostly because of the use of a MHD equation of state and is shown for comparison purpose only. All three stars are on or very close to the theoretical ZAMS at an age of a few 10^7 years, in agreement with their high lithium abundances. A straightforward interpolation within the Schaller et al. tracks suggests masses of 1.10 and 1.07 solar masses for the primary and secondary, respectively, in excellent agreement with the masses from the spectroscopic orbit.

4. A Doppler image for May 2000

4.1. Basic TempMap-code parameters

Our Doppler imaging program (TempMap) is based on the code by Rice et al. (1989) (also described in Piskunov & Rice 1993). Extensive numerical tests and an update of the program's primary capabilities were recently presented by Rice & Strassmeier (2000). For details, we refer the reader to this and previous papers in this series.

As already applied in our previous paper in this series (Rice & Strassmeier 2001, Paper XVII), TempMap can work from a large piece of spectrum and inverts many lines together with two photometric bandpasses simultaneously. The inclusion of large portions of continuum with basically no stellar surface information requires the additional input of a weight for each of the 3155 pixels in the spectrum of σ^2 CrB. We used a program that allowed us to assign weight 0 to the pixels that represented extended regions of continuum (or at least only extremely weak lines) with no information about the stellar surface structure at any phase and weight 1.0 to those regions with line profile information of significance for at least some of the phases during the binary star orbital period.

4.2. The TempMap binary-star version

For the present paper, TempMap was extended to work with two spherical stars in a close binary system. It inverts the line profiles of both stars in the combined spectrum simultaneously. Figure 6 shows an example of a test inversion with a rather complicated and also different surface pattern for the two stars and a maximum-entropy regularization. No photometry was used as input in this case. Figure 7 shows another two reconstructions, now with photometric input in two bandpasses added, one for a Tikhonov regularization and one for a maximum-entropy regularization. Note that in both figures the lower ones in the images are from a smaller secondary star (0.7 times the diameter of the primary star).

One obvious test behavior that is correctly reconstructed is that if the secondary star is both smaller and cooler, the contribution to the spectrum and to the photometry is much less than for the primary. Therefore, the program reacts by simply giving less resolution on the recovery rather than excessive and likely spurious detail. We would expect that in the case where there is significant external and internal error in the input data that a situation like this will result in significantly poorer results (resolution) for the secondary star. This is obviously just due to a lack of information for the weaker secondary.

Another test behavior shows that there appears spurious detail that tends to show up on the primary when there is no penalty function. We suspect that it may have to do with confusing spectrum data that arises from the surface of the secondary star. In such cases, TempMap is trying to interpret the confusing data by adding extra detail to the surface of the primary star first.

4.3. Input parameters for the σ^2 CrB application

The radiative transfer in our program is based on ten LTE plane-parallel model atmospheres with temperatures from 3500 K to 6500 K taken from the ATLAS-9 grid (Kurucz 1993). A gravity of $\log g = 4.5$, a microturbulence of 2 km s^{-1}, and a macroturbulence of 4 km s^{-1} were adopted for both components based on their ≈G0V spectral classification. Further stellar parameters are listed in Table 2. The orbital input parameters are the same as listed in Table 3.

All inversion were set to include a minimum of regularization, sometimes even no regularization at all. With the large number of profiles and phases, the fitting error was always ≈20% larger than the photon noise in the data. Obviously,

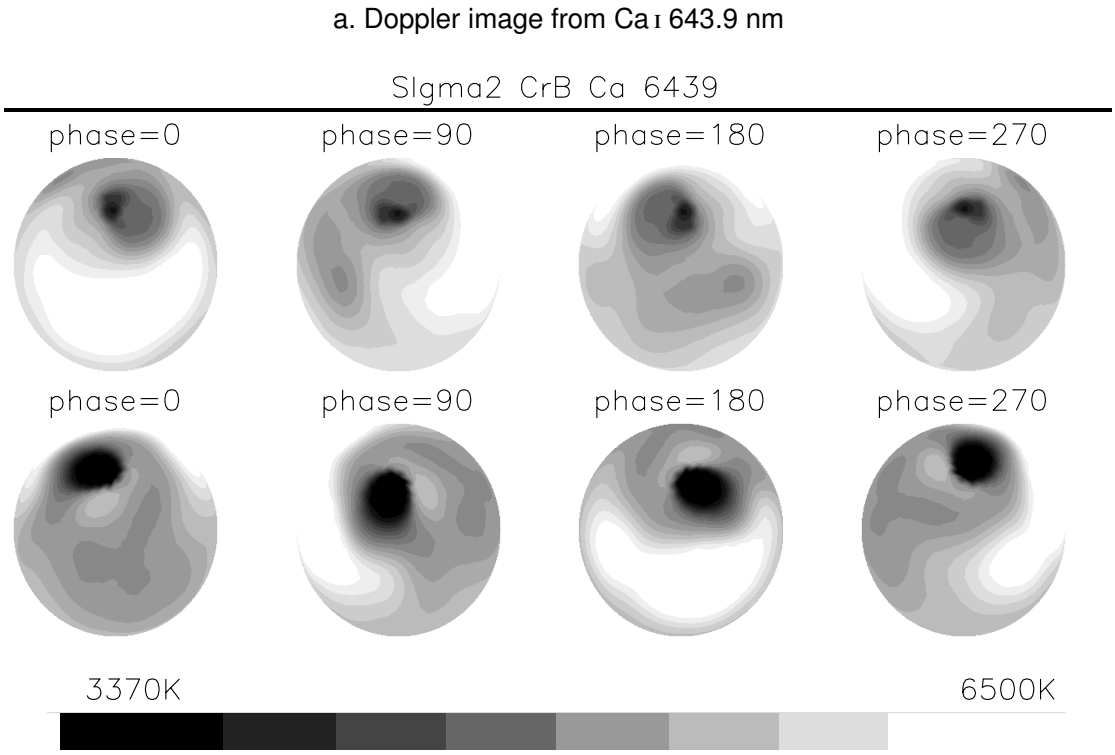

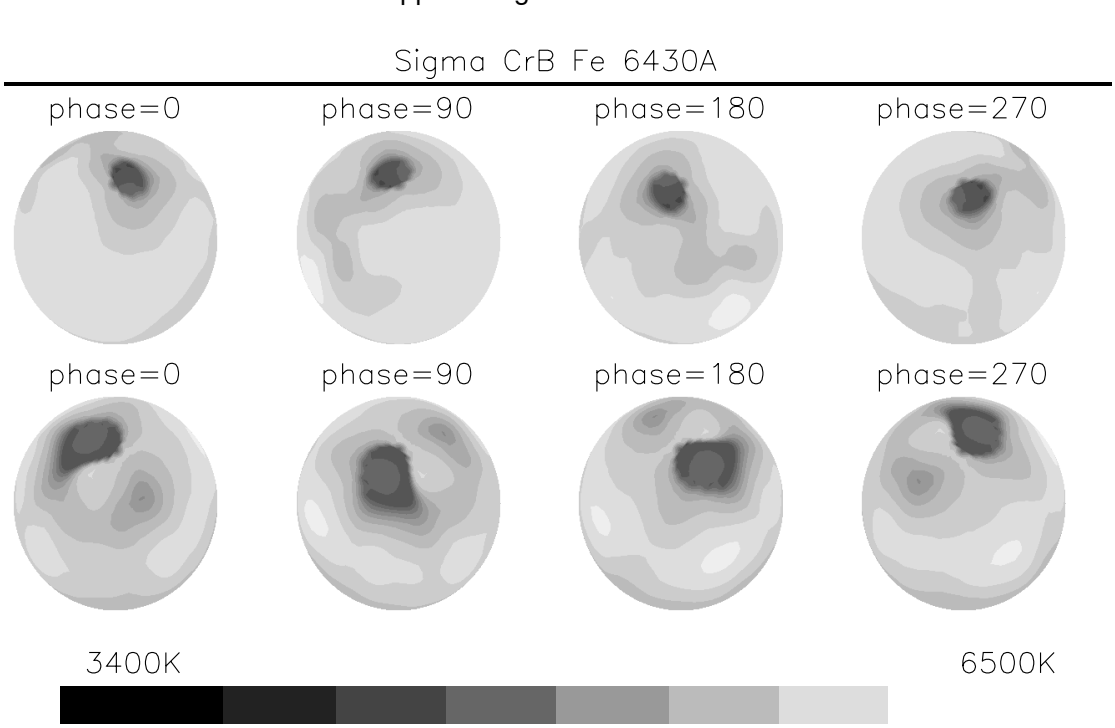

Fig. 8. Doppler images of σ^2 CrB from **a)** Ca I 643.9 nm and **b)** from Fe I 643.0 nm. Top rows represent the primary, bottom rows the secondary.

for σ^2 CrB the photon noise is not the limit for the reconstruction quality but rather the sum of the external errors (see the inversion tests in Rice & Strassmeier 2000). The final maps were nevertheless computed with a minimum amount of (Tikhonov) regularization in order to balance between fitting tiny profile changes due to external errors and real surface detail. Fitting errors were for Ca I 6439 $5.25\,10^{-3}$ (appropriate to $S/N \approx 190:1$), for Fe I 6430 5.54×10^{-3} (appropriate to $S/N \approx 180:1$), and for the full-spectrum fit 5.1×10^{-3} (appropriate to $S/N \approx 200:1$). Error is defined here as $\sqrt{\sum(\mathrm{O-C})^2/(N-1)}$ where N is the total number of spectrum

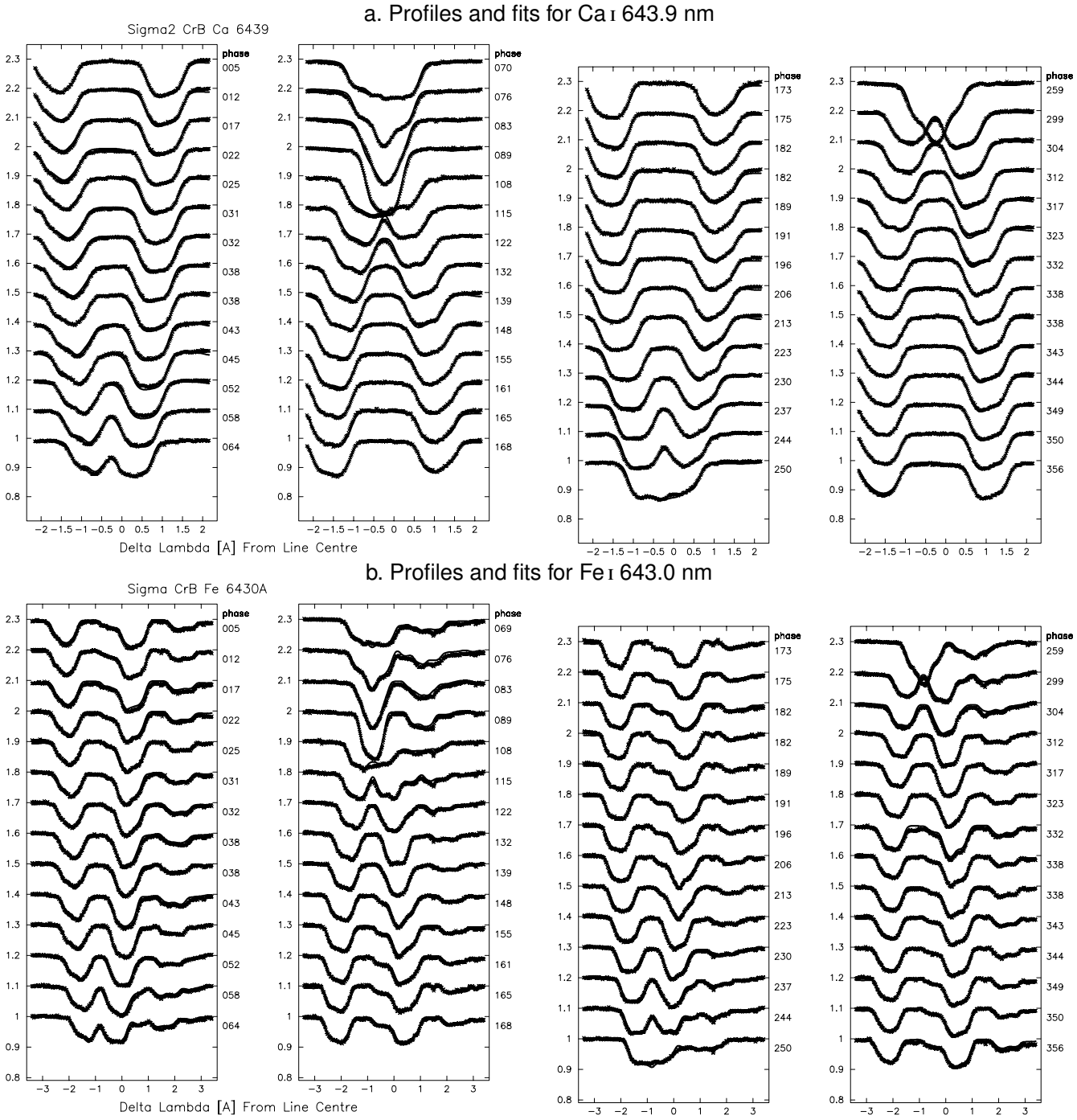

Fig. 9. Observations and fits from the inversion of, **a)** the Ca I 643.9-nm profile and, **b)**, the Fe I 643.0-nm profile.

points in all of the observations, i.e. the number of pixels per phase times the number of phases. This number of data points is such that the problem is essentially over-determined and the least-squares fit predominates. We have two to three times as many profile points per star in total as we have pixels (2592) visible on the surface of each star.

The binary version of TempMap additionally requires the input of the relative radii of the two components. We found "best" results when using $R_{\rm sec}/R_{\rm pri} = 0.955$, instead of the heuristic value of 0.965 as suggested in Sect. 3.4. The latter value was based on the spectral classification for both components and its tabulated radii, thus is accordingly uncertain. Our "best" value is well within the upper limits of 0.965 ± 0.15 (see Table 2) and the ratio difference corresponds approximately to a difference in radius of 1% of one component.

The full-spectrum solution considers a total of 171 lines and two continuum bandpasses in the inversion simultaneously. As for the single-line maps, a total of 56 spectra from all phases is used. The atomic data for these lines were taken from VALD (Vienna Atomic Line Database; Kupka et al. 1999) with the exception of the $\log gf$-values for four major neutral iron lines where we found better values in previous papers in this series (6392.54: −4.23; 6393.60: −1.622; 6408.018: −0.668; and 6411.6493: −0.35). Abundances for the many chemical

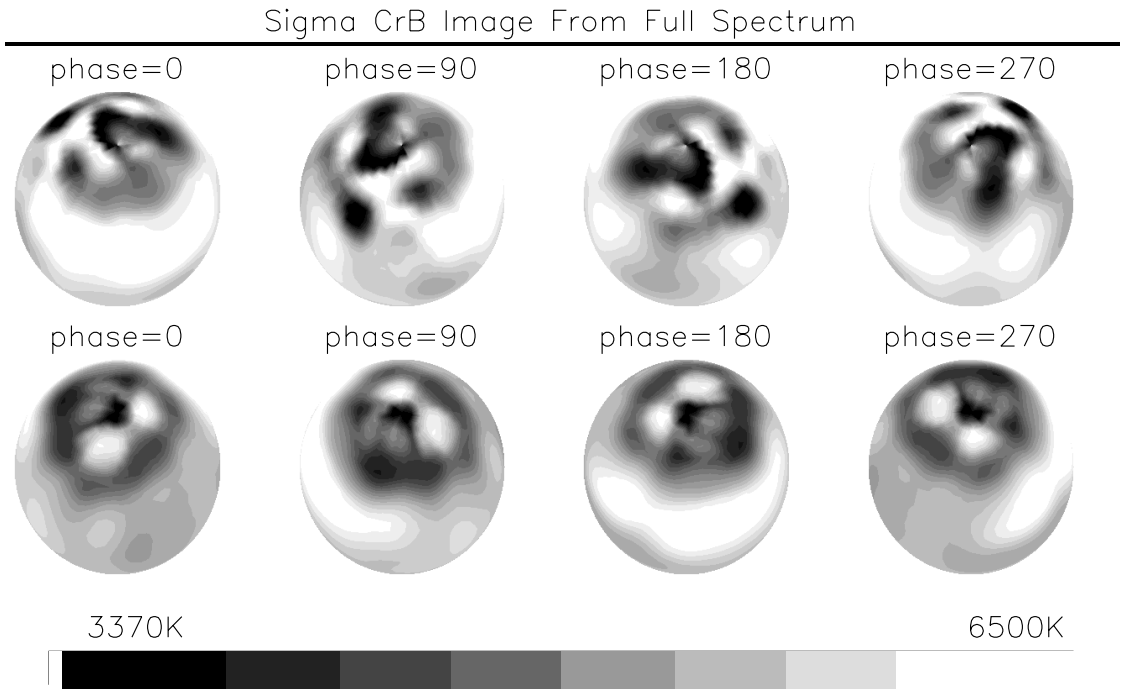

Fig. 10. Doppler image for the primary (top row) and the secondary (bottom row) from the simultaneous inversion of the full 639–645 nm region and two photometric bandpasses.

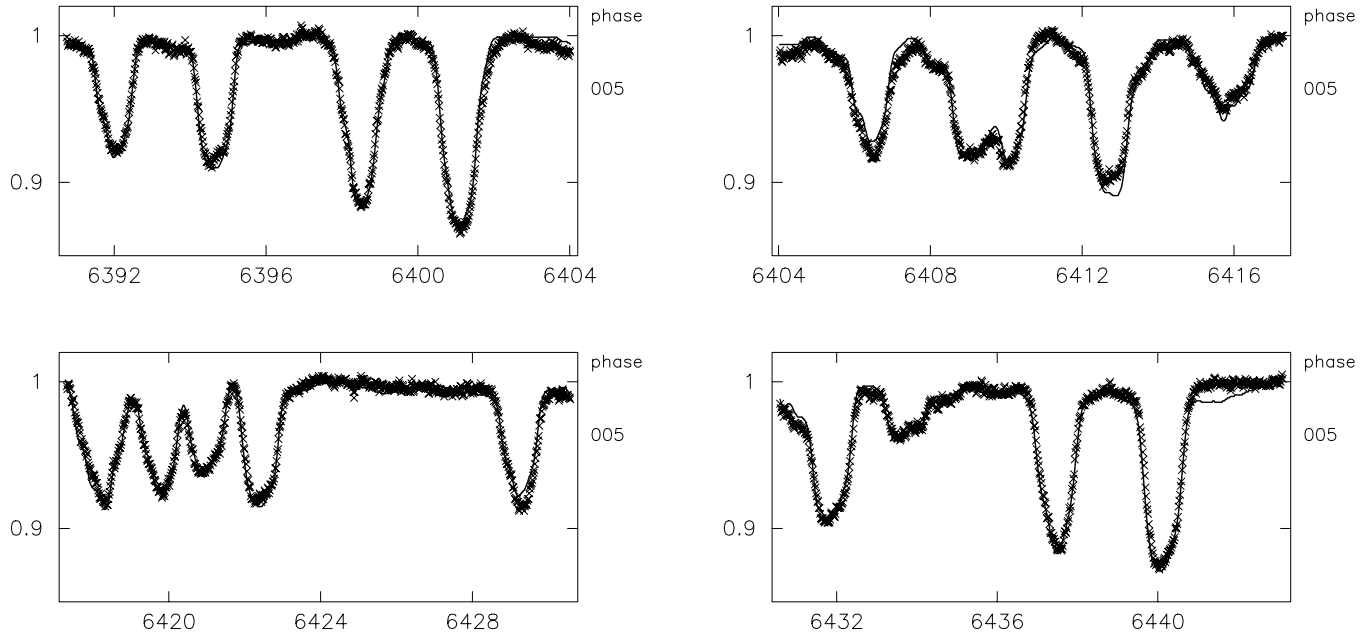

Fig. 11. Example fits for the full-spectrum inversion from Fig. 10. Shown is only one out of the 56 phases (at 5° longitude of the central meridian). The spectral range includes major mapping lines like Ca I 643.9, Fe I 643.0, 642.0, 641.1, and 639.0 nm.

elements within the useable spectral range were kept at the solar value by default but the Fe and Ca abundance were adjusted during the imaging. The values used in the final inversion are 7.30 for iron and 6.07 for calcium (on the regular $\log n(\mathrm{H}) = 12.00$ scale). Both values indicate an underabundance of these two elements relative to the solar photosphere of 0.37 dex ($\approx 4\sigma$) for Fe and 0.29 dex ($\approx 3\sigma$) for Ca. We estimate the external uncertainty of our own determination to be not much better than 0.1 dex but consider the underabundance to be a real effect.

4.4. Results

Figure 8 shows the Doppler images of both components of σ^2 CrB, one set derived from the Ca I 643.9-nm line combination, and one set from the Fe I 643.0-nm combination. Both

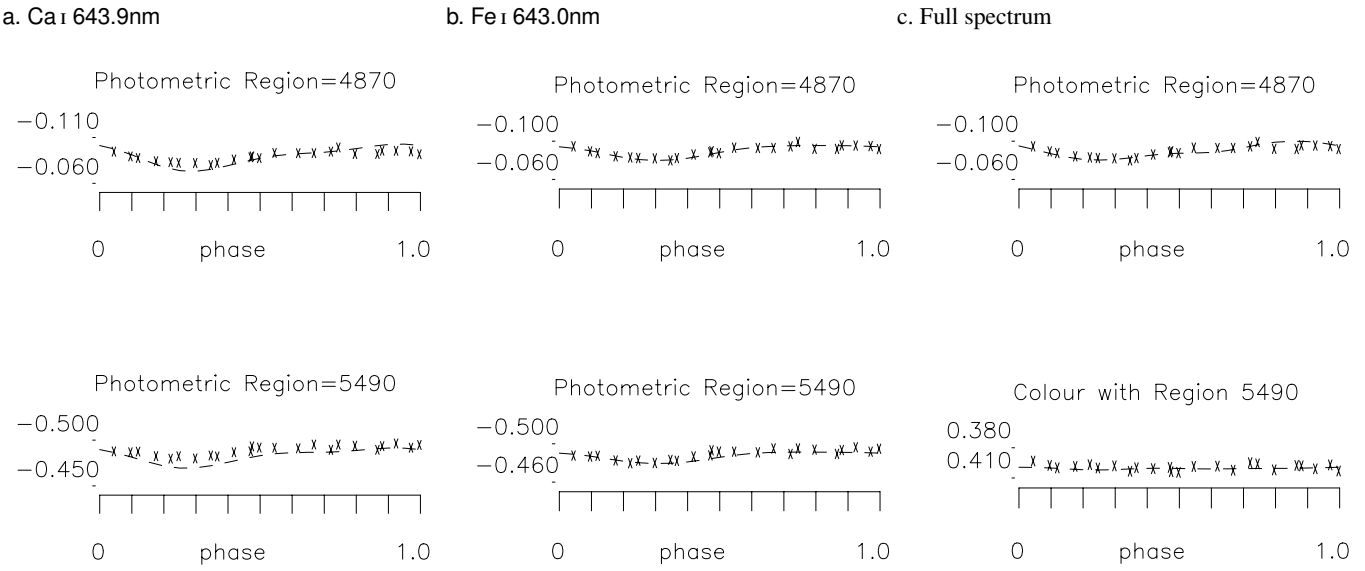

Fig. 12. Combined differential light curves and their fits from the simultaneous solution with the line profiles. **a)** from the Ca-line profiles, **b)** from the Fe-line profiles. The respective upper panels show Strömgren b at an effective wavelength of 487.0 nm, the lower panels show Strömgren y at 549.0 nm. **c)** light and color curve fits from the full-spectrum inversion. Top panel: Strömgren b, bottom panel: $b - y$.

lines unambiguously suggest that both components exhibit a coexistence of cool spots at very high latitudes, possibly even at the pole, and warm spots at low latitudes and the equator. Our test reconstruction did not show any indications that such a phenomenon could be introduced by an image-reconstruction artefact. The image from the Fe-line combination is very similar to the Ca image except for more detail and a smaller temperature contrast between spotted and unspotted regions. This is not surprising since the local line profile for Fe will be narrower than for Ca and thus there will be more resolution elements on the stellar surface. In a certain sense, the Ca maps can be viewed as degraded Fe maps. Furthermore, the positions of both hot and cool features agree nicely in both sets, providing further evidence for their reality. Note that the smaller of the two cool high-latitude spots in the Fe map (on both components) does have a counterpart in the Ca map but at a significantly lower contrast, such that the plots in Fig. 8b barely reveal them. The maximum temperature contrast photosphere minus cool spots is approximately $T \approx 2000$ K on both components. The contrast of the warm features is on average $T \approx -500$ K on both components. The disk-integrated temperatures from our maps are 5966 K for the primary and 5673 K for the secondary. The quality of the data and its fits is shown in Figs.9a and 9b for the Ca-line combination and the Fe lines, respectively. Figures 12a, b show the data and the fits of the combined Strömgren b and y photometry. Note that TempMap not only fits the line profiles and the light-curve shape simultaneously, but also the $b - y$ index.

Figure 10 shows the result from the simultaneous inversion of all spectral information in the full wavelength range of our spectra. Altogether, 171 spectral lines between 639–645 nm (5.2 nm) down to an equivalent width of a few mÅ are included in the inversion. Figure 11 gives an example of the quality of the full-spectrum fit for phase 5° while Fig. 12c shows the fit to the Strömgren b and $b - y$ light and color curve.

5. Discussion and conclusions

The σ^2 CrB surface structure exhibits a complex symmetry within the two stellar components. We demonstrate this in a separate figure (Fig. 13) because it is somewhat difficult to imagine the three-dimensional relations just from the spherical maps in Fig. 8. The phenomenology then appears to be the following:

- Both component's cool high-latitude or "polar" spot appears asymmetric with respect to the star's rotational pole. If viewed as a single feature on both components, respectively (as e.g. from the lower resolution Ca maps) they tend to appear to anti-face each other with respect to the apsidal line (the "anti-facing" hemispheres are the images at 270° for the primary and 90° for the secondary).
- A single cool spot at medium-to-high latitudes appears to exist on the primary facing the secondary.
- A large equatorial warm belt seems to exist on the trailing hemisphere of each of the two stars with respect to the orbital motion (i.e. they appear centered at the central meridian during the respective quadrature phases, and thus are not facing each other as would be the case for a hypothetical reflection effect).
- The leading hemispheres on both components appear with an effectively lower temperature than the trailing hemispheres.

We believe that a meaningful interpretation must involve a strong coupling of the individual stellar magnetic fields and its associated electron acceleration and slowdown along particular field lines. Whether such magnetic coupling in tidally locked stars has an impact on the formation and rise of flux tubes remains to be determined but is suggested from the current results. The recent work of Holzwarth & Schüssler (2000, 2002) already indicates that tidal effects in rapidly-rotating close

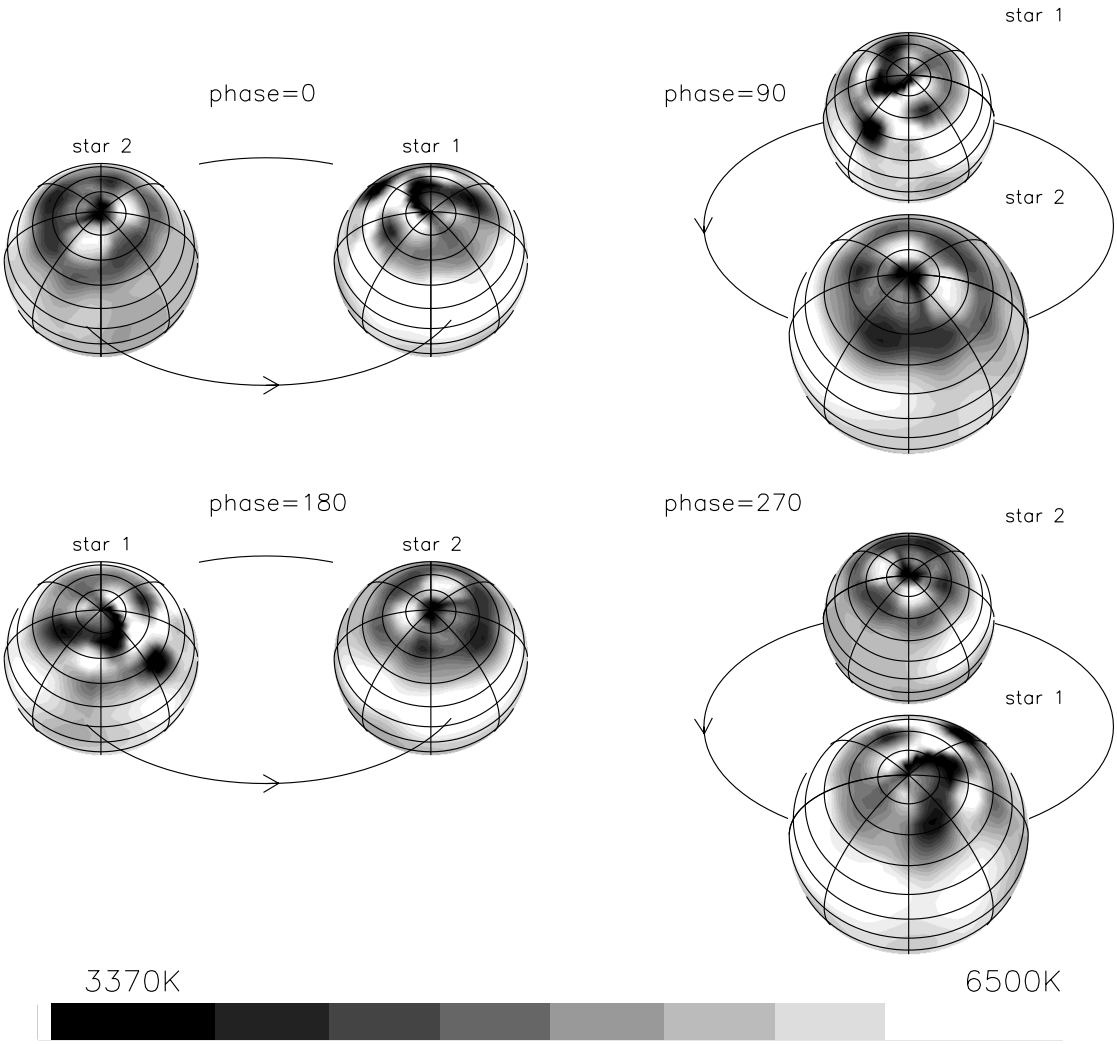

Fig. 13. Pseudo three-dimensional view of the σ^2 CrB binary system. The maps are those from the full-spectrum inversion (see text). Note that the obtained ratio of the stellar radii of the two components is 0.955 but that they are shown at different size during the two conjunction phases (90° and 270°, respectively) for better 3-D viewing.

binaries will cause a considerably non-uniform longitudinal spot distribution. Similar work on single stars by Granzer et al. (2000) and, more recently, by Granzer (2002) allows only solutions symmetric in longitude, but again verify that the rotational period is the dominant parameter in determining the star-spot latitude. Another important factor is the fractional size of the radiative core, while the evolutionary stage and the stellar mass play only a minor role. A recent explanation for the strong differential surface rotation of single active stars involves gravity darkening (Rüdiger & Küker 2002). Due to the rapid rotation a non-uniform heating from below is expected and would cause an equator-ward meridional flow, and thus an acceleration of the equatorial zones. In the case of a rapidly-rotating binary with G or K-components, stellar oblateness of a few percent is not uncommon and gravity darkening should be at work all the time. Whether this mechanism is also sufficient to drive a much stronger meridional flow than on the Sun, that then would move large amounts of magnetic flux to preferred regions – as observed on some systems including σ^2 CrB –, and whether the motion is clockwise or counterclockwise to the stellar rotation are currently open questions that we may solve by providing better observations of systems like σ^2 CrB.

Indeed, a system similar to σ^2 CrB is ER Vulpeculae. It is also a close binary with two synchronized early-G dwarfs (G0V+G2V) but in an even shorter orbit, 0.698 days, which causes partial eclipses at even a moderate inclination. Applying the numerical mapping technique described and tested in Vincent et al. (1993), Piskunov (1996) and Piskunov et al. (2001) presented Doppler images for both components of ER Vul. Hot spots were recovered with $\Delta T \approx 1200$ K above the effective temperature near the sub-stellar points and are presumably due to the reflection effect. Cool regions were also detected on both components but seem to be unrelated to the relative positions of the two stars. A single large feature on the cooler secondary star extends almost across the entire disk. Such enormous cool spots are usually only seen on rapidly-rotating giants. The "record" holder in this context is still the K0 giant in the spectroscopic binary XX Tri (HD 12545) with a single spot ten times the area of the projected solar disk (Strassmeier 1999; for a summary of Doppler images see

Strassmeier 2002). A warm belt on the opposite hemisphere of XX Tri suggests a large-scale bipolarity of the surface magnetic field and local mass exchange from one hemisphere to the other, in principle very similar to our results for σ^2 CrB.

Acknowledgements. KGS is very grateful to the German Science Foundation (DFG) for support under grant STR645/1-1. The APTs were operated from funds from the Austrian Science Foundation grant S7301-AST to kgs until 2001. JBR acknowledges support from the Natural Science and Engineering Research Council of Canada (NSERC).

References

Bakos, G. A. 1984, AJ, 89, 1740
Barker, E. S., Evans, D. S., & Laing, J. D. 1967, ROB No. 130
Barnes, J. R., Collier Cameron, A., Unruh, Y. C., Donati, J.-F., & Hussain, G. A. J. 1998, MNRAS, 299, 904
Barnes, J. R., Collier Cameron, A., James, D., & Donati, J.-F. 2001, MNRAS, 314, 162
Berdyugina, S. V., Berdyugin, A. V., Ilyin, I., & Tuominen, I. 1998, A&A, 340, 437
Berdyugina, S. V., Berdyugin, A. V., Ilyin, I., & Tuominen, I. 1999, A&A, 350, 626
Bradstreet, D. H. 1993, Binary Maker manual
Charbonnel, C., Däppen, W., Schaerer, D., et al. 1999, A&AS, 135, 405
Collier Cameron, A., Walter, F. M., Vilhu, O., et al. 1999, MNRAS, 308, 493
D'Antona, F., & Mazzitelli, I. 1997, R. in Cool stars in clusters and associations, ed. Pallavicini, & G. Micela, Mem. S. A. It. 68, 807
Donati, J.-F., & Collier Cameron, A. 1997, MNRAS, 291, 1
Donati, J.-F., Semel, M., & Rees, D. E. 1992, A&A, 265, 669
Duquennoy, A., & Mayor, M. 1991, A&A, 248, 485
ESA 1997, The Hipparcos and Tycho catalog, ESA SP-1200
Fekel, F. C., Strassmeier, K. G., Washuettl, A., & Weber, M. 1999, A&AS, 137, 369
Flower, P. J. 1996, ApJ, 469, 355
Frasca, A., Catalano, S., & Mantovani, D. 1997, A&A, 320, 101
Giménez, A., Ballester, J. L., & Reglero, V. 1986, AJ, 92, 131
Granzer, T., Schüssler, M., Caligari, P., & Strassmeier, K. G. 2000, A&A, 355, 1087
Granzer, T. 2002, AN, 323, 395
Hall, D. S. 1986, ApJ, 309, L83
Hall, D. S. 1991, in IAU Colloq. 130, The Sun and Cool Stars: activity, magnetism, dynamos, ed I. Tuominen, D. Moss, & G. Rüdiger, (Springer, Berlin-Heidelberg), 353
Harper, W. E. 1925, Publ. Dom. Astrophys. Obs., 3, 231
Hatzes, A. P. 1998, A&A, 330, 541
Hatzes, A. P., & Kürster, M. 1999, A&A, 346, 432
Holzwarth, V., & Schüssler, M. 2000, AN, 321, 175
Holzwarth, V., & Schüssler, M. 2002, AN, 323, 399
Kövari, Zs., & Olah, K. 1996, A&A, 305, 811
Kupka, F., Piskunov, N. E., Ryabchikova, T. A., Stempels, H. C., & Weiss, W. W. 1999, A&AS, 138, 119
Kurucz, R. L. 1993, ATLAS-9, CD-ROM #13
Messina, S., & Guinan, E. F. 2002, A&A, 393, 225
Osten, R. A., Brown, A., Ayres, T. R., et al. 2000, ApJ, 544, 953
Osten, R. A., Ayres, T. R., Brown, A., Linsky, J. L., & Krishnamurthi, A. 2002, ApJ, in press
Pavlenko, Ya. V., & Magazzú, A. 1996, A&A, 311, 961
Percy, J. R. 1980, Bull. AAS, 12, 94
Piskunov, N. E. 1996, in IAU Symp. 176, Stellar Surface Structure, ed. K. G. Strassmeier, & J. L. Linsky (Kluwer, Dordrecht), 45
Piskunov, N. E., & Kochukhov, O. 2001, in Lecture Notes in Physics, ed. H. Boffin, D. Steeghs, & J. Cuypers (Springer), 238
Piskunov, N. E., & Rice, J. B. 1993, PASP, 105, 1415
Piskunov, N. E., Vincent, A., Duemmler, R., Ilyin, I., & Tuominen, I. 2001, in 11th Cool Stars, Stellar Systems, and the Sun, ed. J. Garcia Lopez, R. Rebolo, & M. Zapatero Osorio, PASPC 223, CD-1285
Rice, J. B., & Strassmeier, K. G. 2000, A&AS, 147, 151
Rice, J. B., & Strassmeier, K. G. 1996, A&A, 316, 164 (Paper II)
Rice, J. B., & Strassmeier, K. G. 2001, A&A, 377, 264 (Paper XVII)
Rice, J. B., Wehlau, W. H., & Khokhlova, V. L. 1989, A&A, 208, 179
Rüdiger, G., & Küker, M. 2002, A&A, 385, 308
Schaller, G., Schaerer, D., Meynet, G., & Maeder, A. 1992, A&AS, 96, 269
Schmidt-Kaler, T. 1982, in Landolt Börnstein, vol. I/2b, 15
Skillman, D. R., & Hall, D. S. 1978, IBVS, 1529
Strassmeier, K. G. 1996, A&A, 314, 558 (Paper I)
Strassmeier, K. G. 1999, A&A, 347, 225 (Paper XI)
Strassmeier, K. G. 2002, AN, 323, 309
Strassmeier, K. G., & Bartus, J. 2000, A&A, 354, 537 (Paper XII)
Strassmeier, K. G., Boyd, L. J., Epand, D. H., & Granzer, T. 1997, PASP, 109, 697
Strassmeier, K. G., Hall, D. S., Boyd, L. J., & Genet, R. M. 1989, ApJS, 69, 141
Strassmeier, K. G., Hall, D. S., Fekel, F. C., & Scheck, M. 1993, A&AS, 100, 173
Strassmeier, K. G., & Rice, J. B. 2000, A&A, 360, 1019 (Paper XIV)
Tanner, R. W., 1949, Publ. David Dunlap Obs., 1, 471
Unruh, Y. C., Collier-Cameron, A., & Guenther, E. 1998, MNRAS, 295, 781
Vincent, A., Piskunov, N. E., & Tuominen, I. 1993, A&A, 278, 523
Vogt, S. S., Hatzes, A. P., Misch, A. A., & Kürster, M. 1999, ApJS, 121, 547
Wade, G., Donati, J.-F., Landstreet, J., & Shorlin, S. L. S. 2000, MNRAS, 313, 823
Washuettl, A., Strassmeier, K. G., & Collier Cameron, A. 2000, in 11th Cool Stars, Stellar Systems, and the Sun, PASPC 223, ed. J. Garcia Lopez, R. Rebolo, & M. Zapatero Osorio, CD-1308
Weber, M., & Strassmeier, K. G. 2001, A&A, 373, 974 (Paper XV)